Journal of
Materials Chemistry B

ROYAL SOCIETY
OF CHEMISTRY

PAPER

View Article Online
View Journal | View Issue

Cite this: *J. Mater. Chem. B*, 2024, **12**, 2855

Received 22nd October 2023,
Accepted 11th January 2024

DOI: 10.1039/d3tb02488a

rsc.li/materials-b

Preventing biofilm formation and eradicating pathogenic bacteria by Zn doped histidine derived carbon quantum dots†

Vijay Bhooshan Kumar, *[a] Maoz Lahav[a] and Ehud Gazit *[abc]

Bacterial infections are of major medical concern due to antibiotic resistance. Carbon quantum dots (CDs) have emerged as potentially excellent biomaterials for multifunctional applications due to their low toxicity, outstanding water solubility, high fluorescence, and high biocompatibility. All of these properties allow CDs to be exceptional biomaterials for inhibiting the growth of bacteria and stopping biofilm formation due to their strong binding affinity, cell wall penetration, and solubilizing biofilm in water. Here, we describe a strategy for one-pot synthesis of histidine-derived zinc-doped N-doped CDs (Zn-NCDs) by a hydrothermal method for inhibiting the growth of both Gram-positive and Gram-negative bacteria without harming mammalian cells. The NCDs and Zn-NCDs showed uniform sizes (~6 nm), crystallinity, good photostability, high quantum yield (76%), and long decay time (~5 ns). We also studied their utilization for live cell bio-imaging and the antimicrobial properties towards the Gram-positive *Staphylococcus aureus* and the Gram-negative *Pseudomonas aeruginosa*. Importantly, the Zn-NCDs could penetrate the biofilm and bacterial cell wall to effectively inhibit the growth of bacteria and subsequently inhibit biofilm formation. Thus, the structure, chemical composition, and low toxicity properties of the newly-developed Zn-NCDs exemplify a promising novel method for the preparation of nano-level antibacterial drugs.

1. Introduction

Many of the severe clinical problems currently encountered are caused by various bacterial infections.[1] In many cases, multidrug resistance limits the efficacy of conventional antimicrobial agents.[2–4] To overcome these problems, novel types of antibiotic molecules needed for targeting various bacterial features are extensively important. A study conducted by the World Health Organization (WHO) indicates that antimicrobial resistance is one of the top 10 global public health threats and is a leading cause of morbidity and mortality in the world.[5] Antibiotic-resistant strains have significantly increased the number of deaths and severity of bacterial infections such as methicillin resistance which was found to predate the clinical use of antibiotics.[6] It is estimated that the number of deaths caused by antibiotic-resistant bacteria in the world exceeds the number of deaths caused by cancer and diabetes combined.[5] Despite the substantial availability of antibiotics, resistant strains have been identified for almost all of them. It is not uncommon for antibiotic resistance to develop shortly after a new drug has been approved for use.[5] Additionally, rapid and timely detection of infections can prevent bacteria proliferation and the formation of biofilms at the infection site.[7–9] After the biofilm has been formed, bacteria embedded within it will be protected by self-secreted extracellular polymeric substances and will become resistant to the host's immune response as well as antibiotics, resulting in stubborn chronic infections.[7,8] It is therefore imperative to diagnose bacterial infections, destroy biofilms effectively, and develop novel strategies to address the issue of bacterial infections. Among patients in intensive care, bacterial infections are a major cause of increased mortality. In particular, bacterial co-infections and secondary infections are common in COVID-19 positive patients,[10] as well as in patients suffering from skeletal infections[11] and healthcare-associated pneumonia.[12] Thus, finding new antimicrobial preparations is a high-priority task of public health worldwide.

Carbon quantum dots (CDs) have attracted significant attention in recent years due to their potential for a wide range of applications, including biomedical engineering,[13] sensor technology,[14,15] fluorescent labelling and cell imaging,[16] dye

---

[a] *The Shmunis School of Biomedicine and Cancer Research, George S. Wise Faculty of Life Sciences, Tel Aviv University, 6997801, Tel Aviv, Israel. E-mail: ehudga@tauex.tau.ac.il, vijaybhushan86@gmail.com*

[b] *Department of Materials Science and Engineering Iby and Aladar Fleischman Faculty of Engineering, Tel Aviv University, Tel Aviv 6997801, Israel*

[c] *Sagol School of Neuroscience, Tel Aviv University, Tel Aviv 6997801, Israel*

† Electronic supplementary information (ESI) available: Online Library or from the author. See DOI: **https://doi.org/10.1039/d3tb02488a**

degradation or photocatalysts,[17] chemiluminescence,[18] solar cells,[19] nano-electronic devices,[20] COVID-19 treatment,[21] photodynamic therapy,[22] and gene delivery.[23] CDs are nanoscale carbon nanomaterials with dimensions of less than 10 nm in all three dimensions, and are characterized by their persistent fluorescence and high biocompatibility. They can be synthesized using a variety of methods, including arc discharge, laser ablation, hydrothermal solution, electrochemical oxidation, sonochemistry, and microwave technologies.[24] Among these methods, hydrothermal synthesis is particularly attractive due to its simplicity, low cost, and ability to produce a wide range of CDs and doped CDs. In contrast, doped CDs can be tuned by doping the CDs with heteroatoms to alter their optical, electrical, and surface chemical properties.[24] In addition, the surface of doped CDs[25] is typically modified with oxygen, nitrogen, carbonyl, or carboxyl functionalities, which may provide detection properties through strong interactions with non-metal/metal ions.[26] The doping of CDs with metal atoms shows slightly better properties in terms of the incorporation of non-metal atoms into the CDs matrix.[27] Doped CDs with transition metal atoms would result in a change in charge density and a transition between graphene matrix and metal ions with its tremendous electron mobility, which is expected to alter the physical properties of CDs.[27] It is possible, however, that doping the CDs with a metal atom may result in their toxicity. Therefore, the dopant should be environmentally-friendly and non-toxic to cells. Specifically, zinc, one of the most important transition metals, encompasses a wide variety of electron transfer processes in the environment, as well as serves as an important co-factor for a variety of biosystems in our ecosystem.[28] Indeed, zinc deficiency can result in several health complications and diseases.[29] Hence, using Zn as a dopant for CDs may be beneficial for improving the properties of carbon nanomaterials without increasing their toxicity.

Many metals and their ions are known to have antimicrobial properties.[30] Silver and copper have been used for their antimicrobial properties in ancient civilizations, and other metals such as zinc, aluminium, and iron have also been shown to have antimicrobial activity.[31,32] The mechanisms behind the antimicrobial properties of metals include the ability to inhibit enzymes, generate reactive oxygen species, damage cell membranes, and prevent the uptake of essential microelements by microbes.[33,34] Moreover, Zinc is an essential micronutrient for many organisms, including bacteria.[35] However, high concentrations of zinc or certain forms of zinc can have toxic effects on bacteria.[36] Zinc ions (Zn^{2+}) can disrupt bacterial cell membranes and interfere with essential cellular processes.[37] They can interact with sulphur-containing proteins and enzymes, leading to denaturation and loss of function.[38,39] Zinc-based antimicrobial materials, such as zinc oxide nanoparticles and zinc complexes, are well-established and have a wide range of applications.[40–43] In hospital-acquired infections, zinc ions accelerate the inhibition of *Streptococcus pyogenes* and induce intercellular adhesion of *Staphylococcus epidermidis* and *Staphylococcus aureus*.[44–46] Furthermore, zinc ions are bound to a significant number of proteins, mostly through a combination of histidine residues.[39,47,48] The side chains of histidine molecules are capable of donating or accepting hydrogen bonds from other groups in addition to atoms that coordinate directly to zinc ions.[48] In all living organisms, histidine plays a variety of roles, including acting as a key mediator of the interactions between biomolecules and inorganic compounds.[49] Therefore, we have chosen histidine as a source for generating CDs with zinc metal doping.

The synthesis of histidine-derived N-doped CDs (NCDs) for bio-imaging was previously presented,[50] but there have been no reports on the eradication of highly pathogenic bacteria. Histidine-derived NCDs are a multipurpose class of biomaterials with notable biological and chemical properties.[50] To improve their antimicrobial properties through the discovery of new structures, here we designed and synthesized novel zinc-doped NCD complexes. We describe a facile hydrothermal synthesis method for preparing fluorescent histidine-derived Zn-doped NCDs (Zn-NCDs) which show excitation-dependent fluorescence. The method does not require any additives (such as acids, alkalis, or salts), organic solvents, or further surface modification/passivation. The NCDs and Zn-NCDs were characterized by transmission electron microscopy (TEM), UV-visible spectroscopy, fluorescence spectroscopy, X-ray photoelectron spectroscopy (XPS), and energy-dispersive spectrometry (EDS). The NCDs and Zn-NCDs showed uniform sizes, crystallinity, good photostability, and high solubility in aqueous media. The results of UV-visible, XPS, and EDS spectrometry confirmed their chemical composition. Importantly, the Zn-NCDs could penetrate biofilm and also bacterial cell walls to effectively inhibit the growth of bacteria and subsequently inhibit biofilm formation. Furthermore, the antibacterial effect of Zn-NCDs was found to be slightly better than NCDs. We also studied their live cell bio-imaging properties and antimicrobial activity against Gram-positive *Staphylococcus aureus* (*S. aureus*) and Gram-negative *Pseudomonas aeruginosa* (*P. aeruginosa*).

2. Material and methods

2.1. Materials

Histidine (99% (TLC)), Crystal violet (90.0%, anhydrous basis), Quinine sulphate (98.0%) and Zinc nitrate (≥99.8%) were purchase from Sigma-Aldrich Co., Ltd, Israel. All materials were used without further purification.

2.2. Synthesis of water-soluble Zn-NCDs

Our previously described hydrothermal method was employed with modifications, as follows.[51] Briefly, a homogeneous histidine aqueous solution was prepared by dissolving 500 mg histidine molecules in 70 mL deionised water to a final concentration of ∼50 mM. Homogenous 20 mL of the histidine solution was supplemented with different amounts of Zn ion (0.5 mM to 50 mM) and was then moved to a 50 mL of Teflon-lined autoclave and heated at 200 °C for 8 h in a hot air oven. Upon cooling the autoclave at 25 °C, a dark yellowish-brown liquid was obtained. The small portion of carbide slag was discarded from the product solution by Millipore filtration (0.22 μm).

The solution then was dialyzed against deionised water through Amicon® Ultra-15 Centrifugal Filter Units (M_{WCD} = 2000 Da) to remove the unreacted histidine and Zn ion from the solution. A control sample was synthesized without Zn doping using the same procedure and precursors to yield NCDs. The finally obtained pale yellow-brown aqueous solution of Zn-NCDs/NCDs was evaluated by physico-chemical techniques and subsequently exploited for checking the effect on killing the bacterial growth and biofilm formation as well as live cell imaging of bacterial cell growth and HeLa cell. Zn-NCDs/NCDs was characterized using various physical and chemical techniques and tested for its ability to inhibit the growth of bacteria and biofilm formation, as well as its suitability for live cell imaging of bacterial cell growth and HeLa cells.

2.3. Analytical tools

Fluorescence spectroscopy measurement: 2 mL sample solution was pipetted into a 1.0 cm path-length quartz cuvette, and the spectrum was collected using a FluoroMax-4 Spectrofluorometer (Horiba Jobin Yvon, Kyoto, Japan) at ambient temperature. The excitation and emission wavelengths were set at 320–540 nm and 350–850 nm, respectively, with a slit of 2 nm. UV-visible analysis of the NCDs/Zn-NCDs was performed using a spectrophotometer (Varian Cary 100). The morphology and crystalline properties of NCDs/Zn-NCDs were analysed by high-resolution transmission-electron microscopy (HR-TEM, JEOL 2100). EDS analysis was performed after drying using lyophilization. EDS analysis of Zn-CQDs was measured using HR-TEM (JEOL 2100) attached EDS spectrometer with a monochromatic X-ray source of Al Kα excitation. X-XPS was recorded using an ESCALAB QXi X-ray Photoelectron Spectrometer Microprobe spectrometer with a monochromatic X-ray source (Micro-focused dual-anode Al K-Alpha and Ag L-Alpha source) with Al Kα excitation (1486.6 eV), using C 1s as reference energy (EC 1s = 284.0 eV). The X-ray diffraction (XRD) for the synthesized NCDs and Zn-NCDs powder sample were recorded using Bruker D8 advance XRD with Cu Kα radiation (γ = 0.154 nm wavelength).

The quantum yield of histidine-derived NCDs and Zn-NCDs was determined by comparing the photoluminescence intensities (excited at 360 nm) and absorbance values (at 360 nm) of Zn-NCDs and NCDs with that of quinine sulfate (in 0.1 M H_2SO_4 (quantum yield = 54%). The emission spectra at 360 nm were used to obtain the integrated fluorescence intensity, which is the area under the photoluminescence curve over the wavelength range from 370 to 700 nm. Next, the integrated fluorescence intensity was plotted against the absorbance. According to the following equation, quantum yield values were calculated:

$$\mathrm{QY} = \mathrm{QY}_{\mathrm{st}}\frac{A_{\mathrm{x}}}{A_{\mathrm{st}}} \times \frac{\mathrm{PL}_{\mathrm{st}}}{\mathrm{PL}_{\mathrm{x}}} \times \frac{{n_{\mathrm{x}}}^2}{{n_{\mathrm{st}}}^2} \times 100\% \qquad (1)$$

where the subscripts st and x indicate the quinine sulfate standard and NCDs/Zn-NCDs, respectively. Fluorescence quantum yield is defined as QY, A is the absorbance, PL is the area of peak photoluminescence emission, and n is the refractive index of the solvent (both refractive indices are 1.33). The absorbance at 360 nm in a 10 mm cuvette was kept below 0.1 OD to minimize re-absorption effects.

2.4. Cell viability measurement

MTT assay was performed using human cervical carcinoma (HeLa) cells. Cells were seeded in 96-well microtiter plates and allowed to attach overnight at 37 °C under 5.0% CO_2. The cells were then washed with pH 7.4 PBS buffer and incubated with MTT solution for 3.5 h. Thereafter, the MTT reagent was discarded and 100 μL of DMSO was added to each well to dissolve formazan crystals. The absorbance was recorded using a microplate reader at 570 nm. Control experiments were conducted in the absence of NCDs/Zn-NCDs. All the experiments were carried out in quadruplicates.

2.5. Live cells imaging of bacterial cell and mammalian cell

using confocal microscopy of bacterial cells was performed after grown into a glass cell culture test tube. The bacteria cell was cultured with 100 μg mL^{-1} of Zn-NCDs-containing LB media for different durations. The bacterial cells were then washed twice with PBS and recorded the confocal microscopy. Imaging was performed using SP8 inverted confocal microscope (Leica Microsystems, Wetzlar, Germany). Excitation and emission ranges were λ_{ex} = 480 nm, λ_{em} = 500–580 nm. Similarly, the live HeLa cell with NCDs/Zn-NCDs were obtained using confocal microscopy. In brief, the HeLa cells were grown in glass bottom dishes until they reached 70 to 80% confluence. Afterward, the cells were treated with NCDs/Zn-NCDs at a concentration of 100 μg mL^{-1}. After that, the cells were washed twice with PBS. Imaging was performed using SP8 inverted confocal microscope (Leica Microsystems, Wetzlar, Germany). Excitation and emission ranges were λ_{ex} = 480 nm, λ_{em} = 500–580 nm.

2.6. Bacterial culture and assays

Pseudomonas aeruginosa and *Staphylococcus aureus* were cultured in Luria-Bertani (LB) broth medium. A single colony of each bacterium was selected from a LB agar plate and incubated in 5 mL of LB culture medium at 37 °C for 12 hours at 180 rpm. The concentration of bacteria was determined by measuring the optical density at 600 nm (OD_{600}) and kept below 0.03 for bacterial culture. Therefore, the overnight bacterial cell culture was diluted 1:100 in LB with or without different concentrations of NCDs/Zn-NCDs and then inoculated into 96-well plates with 100 μL per well. The inoculated plates were incubated for 24 hours at 37 °C without shaking and OD_{600} was recorded. In addition, the anti-bacterial of NCDs/Zn-NCDs was also evaluated using the colony forming unit (CFU) counting method. *S. aureus* and *P. aeruginosa* in log phase were cultured in 1/5 LB containing 60 μg mL^{-1} of NCDs/Zn-NCDs at 37 °C for 24 hours. Furthermore, antibacterial activity of NCDs/Zn-NCD nanomaterials was tested against *S. aureus* (a Gram-positive bacterium) and *P. aeruginosa* (a Gram-negative bacterium) using the agar well diffusion method. In detail, in the disk-diffusion method, the agar plate surface is inoculated by spreading 100 and 200 μL of inoculum against *S. aureus* and *P. aeruginosa* bacteria over the entire surface. A circular parchment paper with a diameter of 7 mm has punched aseptically with a sterile cork borer, and these cut parchment papers were autoclaved. Then, autoclaved sterile several parchment papers were soaked in 1 mL of NCDs/Zn-NCDs solution, and these soaked papers were introduced into the bacterial culture on both agar plates. After that, the agar plates are incubated at 37 °C for 24 hours. It has been shown that NCDs/Zn-NCDs substances diffuse in an agar medium and inhibit the growth of microbial strains.

2.7. TEM characterization of bacterial cells

A 10 ug mL^{-1} mixture of NCDs or Zn-NCDs nanomaterials was added to *S. aureus* and *P. aeruginosa* cultures as described in the bacterial culture and assays experiments (Section 4.6). Then, the bacteria cells were collected by centrifugation and fixed with 2.5% glutaraldehyde and paraformaldehyde at 4 °C for 2 hours. The sample was washed for 30 minutes in a 0.1 M PBS solution. Bacterial cells were then dropped on a carbon-coated Cu TEM grid and analysed by TEM.

2.8. Biofilm activity

Assays for the detection and formation of biofilms were adapted from previous procedures.[52] A suspension containing 5×10^7 CFU per mL of *S. aureus* and *P. aeruginosa* with 1% glucose was prepared, followed by inoculating 96-well flat-bottomed non-tissue culture plates with 100 μL of either bacterium or a mixture of both cultures. The biofilm was allowed to form for 24 hours in an anaerobic incubator (atmosphere of 5% CO_2, 10% H_2, 85% N_2, 37 °C). *S. aureus* and *P. aeruginosa* non-adherent bacteria were removed from the 96-well plate by three washings it with phosphate-buffered saline (PBS). Subsequently, 100 μL of methanol were added to each well for 10 mins to fix the biofilms. As soon as the plate had been fixed, it was washed three times in distilled water and air-dried at room temperature for 30 mins, stained with 1% crystal violet (Sigma-Aldrich, USA), and rinsed thoroughly with PBS until the negative control wells appeared colourless. The plate was then decoloured with 150 μL 95% (v/v) ethanol and the absorbance was determined by measuring the OD using a microplate reader.

2.9. Inhibition of biofilm formation by NCDs/Zn-NCDs nanomaterials

Flat-bottomed tissue culture 24-well plates were prepared with autoclaved cover glass slide placed at the bottom of the well and inoculated with 500 μL of liquid suspensions of *S. aureus* and *P. aeruginosa* in an anaerobic incubator for 24 h, followed by measurement of absorbance, as outlined above (Section 2.3). Then, the plates were treated with varying levels of NCDs/Zn-NCDs (0 to 50 μg mL^{-1}), followed by fluorescence microscopy.

3. Results and discussion

3.1. Physical and chemical properties

Histidine has amino and carboxylic acid groups, allowing a variety of nitrogen and oxygen functionalities within the NCDs shell, while Zn also provides Zn doping. During hydrothermal reaction of aqueous solution of histidine (Fig. 1a), hydrogen bonds are formed between the two histidine's. Next, the polymerization process occurs after the histidine polymer is heated and dehydrated, resulting in a short burst of nucleation. Consequently, nuclei are formed by the diffusion of solutes toward the surfaces of NCDs. We propose the polymer carbon skeleton as a crosslinking agent after dehydration. Upon carbonization, a fraction of the precursors is consumed in order to further modify the carbon core.

NCDs doped with different concentrations of Zn was visually inspected and compared to control samples (distilled water, aqueous solution of histidine, Zn ion, and NCDs alone) A transparent aqueous solution containing NCDs and Zn-NCDs exhibited a pale-yellow colour in daylight and a blue-green colour under UV light (Fig. 1b), clearly showing the changes in the colour of the solution following doping with Zn. Moreover, histidine, water, and Zn ion controls did not exhibit any fluorescence, whereas NCDs and Zn-NCDs exhibited a high level of fluorescence under UV light illumination (Fig. 1b). The absorption spectrum of Zn-NCDs *versus* the control samples is shown in Fig. 1c and d. The as-prepared histidine-derived NCDs exhibited a distinct characteristic peak of π–π* transition of the C═C group at 290 nm and a shoulder peak at 350 nm, which were attributed to the n–π* transition of the C═O group. When Zn ion concentrations were elevated from 0.1 wt% to 5 wt%, a slight broadening of the shoulder peak absorption band was observed. Additionally, Zn-NCDs and NCDs showed almost similar absorption characteristics with the exception of a slight increase in peak intensities at their respective wavelengths upon increasing Zn concentrations. In comparison with the control samples, Zn-NCDs showed a slightly higher absorption intensity (hyperchromic effect). Accordingly, it can be concluded that the UV-visible absorption shift toward lower wavelengths and higher intensity supports the doping of Zn ions or metallic Zn within the carbogenic surface of the NCDs nanomaterials to produce highly emissive excitation-dependent Zn-NCDs nanomaterials. We analysed the photoluminescence characteristics of histidine-derived NCDs and Zn-NCDs at various excitation wavelengths (λ_{ext} = 320–540 nm) using a fluorescence spectrometer. The fluorescence emission spectra of NCDs and Zn-NCDs showed narrow bands with maximum emission between 450 and 500 nm (Fig. 1e–k). In the case of CDs and doped CDs, two fluorescence mechanisms have been proposed: electronic conjugated structures and emission traps.[53] The fluorescence behaviours of NCDs/Zn-NCDs are similar to those of previously reported CDs.[51] A fluorescence spectrum of NCDs is shown in Fig. 1e, and characteristic fluorescence spectra of Zn-NCDs of different compositions are shown in Fig. 1f–k. We observed a maximum fluorescence emission intensity between 470 and 500 nm when NCDs and Zn-NCDs were excited at 380–400 nm, which indicates a relatively narrow particle size distribution. In the same way, we measured the fluorescence of an aqueous solution of histidine molecules, but only detected negligible fluorescence, which is much lower than the histidine-derived NCDs (Fig. S1, see the ESI†).

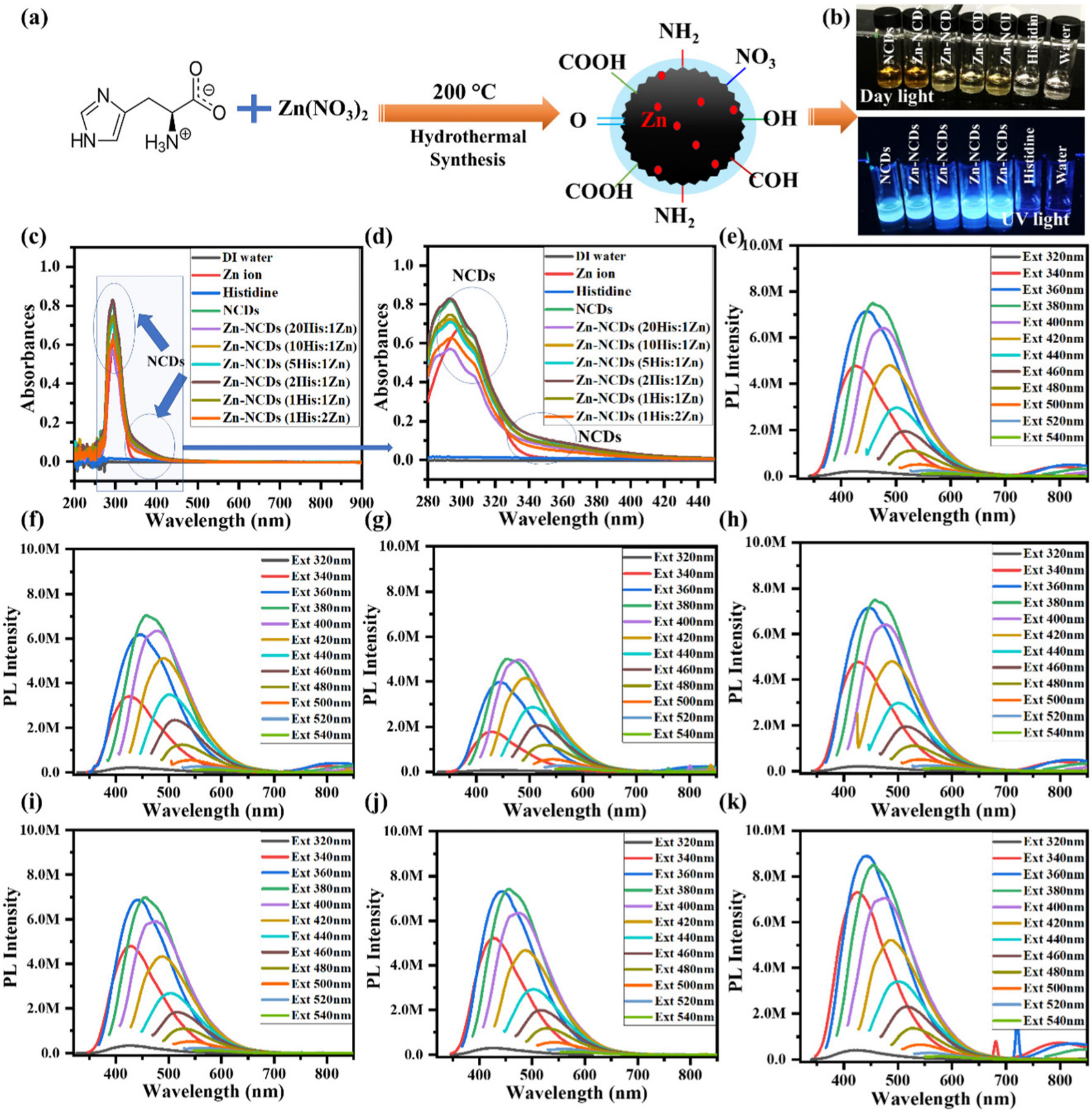

Fig. 1 (a) Schematic presentation of synthesis of water-soluble NCDs/Zn-NCDs. (b) Photographs of the control solutions (deionized water, aqueous solution of histidine, Zn ions, and NCDs) and Zn-NCDs containing different Zn concentrations under daylight and UV light. (c) and (d) UV-visible spectra of NCDs and Zn-NCDs with different concentrations of Zn ion along with deionized water and Zn ion only as control samples. (c) Complete UV-visible spectra (200–900 nm). (d) Magnified *y*-axis part (280–450 nm) of images of Fig. 1c. (e)–(k) Fluorescence spectra of (e) NCDs, (f) Zn-NCDs (20 His:1 Zn ions), (g) Zn-NCDs (10 His:1 Zn ions), (h) Zn-NCDs (5 His:1 Zn ions), (i) Zn-NCDs (2 His:1 Zn ions), (j) Zn-NCDs (1 His:1 Zn ions), and (k) Zn-NCDs (1 His:1 Zn ions) at various excitation wavelengths (λ_{ex} = 320–540 nm).

Table 1 Several different ratios of zinc and histidine were used to produce Zn-NCDs with fluorescence yield, Zn doping amount, and cytotoxicity

Starting materials	Product	By product (in the form of ppt)	Fluorescence QY	Doping level of Zinc by XPS and EDS	Cytotoxicity (100 μg mL^{-1})
Histidine only + H_2O	NCDs	Scarce carbon slag	74	0 wt%	No toxic
20 Histidine: 1 Zn + H_2O	Zn-NCDs	Scarce carbon slag	72	Not measured	No toxic
10 Histidine: 1 Zn + H_2O	Zn-NCDs	Less carbon slag	70	2.3 wt%	No toxic
5 Histidine: 1 Zn + H_2O	Zn-NCDs	More carbon and Zn slag	76	5.2 wt%	Slightly toxic
2 Histidine: 1 Zn + H_2O	Zn-NCDs	More carbon and Zn slag	70	Not measured	Slightly toxic
1 Histidine: 1 Zn + H_2O	Zn-NCDs	More carbon and Zn slag	62	Not measured	Toxic
1 Histidine: 2 Zn + H_2O	Zn-NCDs	More carbon and Zn slag	53	Not measured	Toxic

Table 1 summarizes the properties of the Zn-NCDs nanomaterials produced using different ratios of histidine and zinc. The 10 histidine: 1 Zn showed high fluorescence, reduced Zn doping, and non-toxicity, indicating it as a potentially useful good material for biomedical applications. In addition, we observed more slag or by-product formation when Zn-doping at high concentrations (more than 10 : 1 His : Zn 1 zinc in 10 histidine), which was removed by centrifugation and filtration during synthesis. We, therefore, proceeded with the measurement of Zn-NCDs synthesized from 10 : 1 His : Zinc (which produces 2 wt% of Zn-containing Zn-NCDs), compared to pristine NCDs (without Zn doping).

While NCDs alone had quantum yields of 74% (compared to quinine sulphate), by Zn-doping to form Zn-NCDs, this yield could be increased up to 76 (Fig. S2, ESI†). As shown in Fig. S3 (ESI†), NCDs and Zn-NCDs fluorescence lifetimes were measured using time-correlated single photon counting (TCSPC) to be 4.19 ns and 4.47 ns, respectively (Fig. S3, ESI†). It was found that the lifetime of the Zn-NCDs (Fig. S3c and d, ESI†) is slightly higher than NCDs (Fig. S3a and b, ESI†), indicating that the Zn surface functional groups were indeed present in the Zn-NCDs nanomaterials and exhibited little variation in term of fluorescence and quantum yield.

In order to investigate the chemical composition of the NCDs and Zn-NCDs materials, XPS measurements were conducted. The XPS spectra shown in Fig. 2 clearly demonstrate that carbon, nitrogen, and oxygen were present on the surface of NCDs nanomaterials, with a distribution of C_{1s} (65.8%), N_{1s} (17.5%), O_{1s} (15.7%), and Zn_{2p} (0.0%). The binding energy peak at 284, 399, and 531 eV shown in Fig. 2a corresponded to the typical XPS survey peaks at C_{1s}, N_{1s}, and O_{1s}, respectively. Fig. 2b shows the high-resolution C1s spectrum, with peaks at

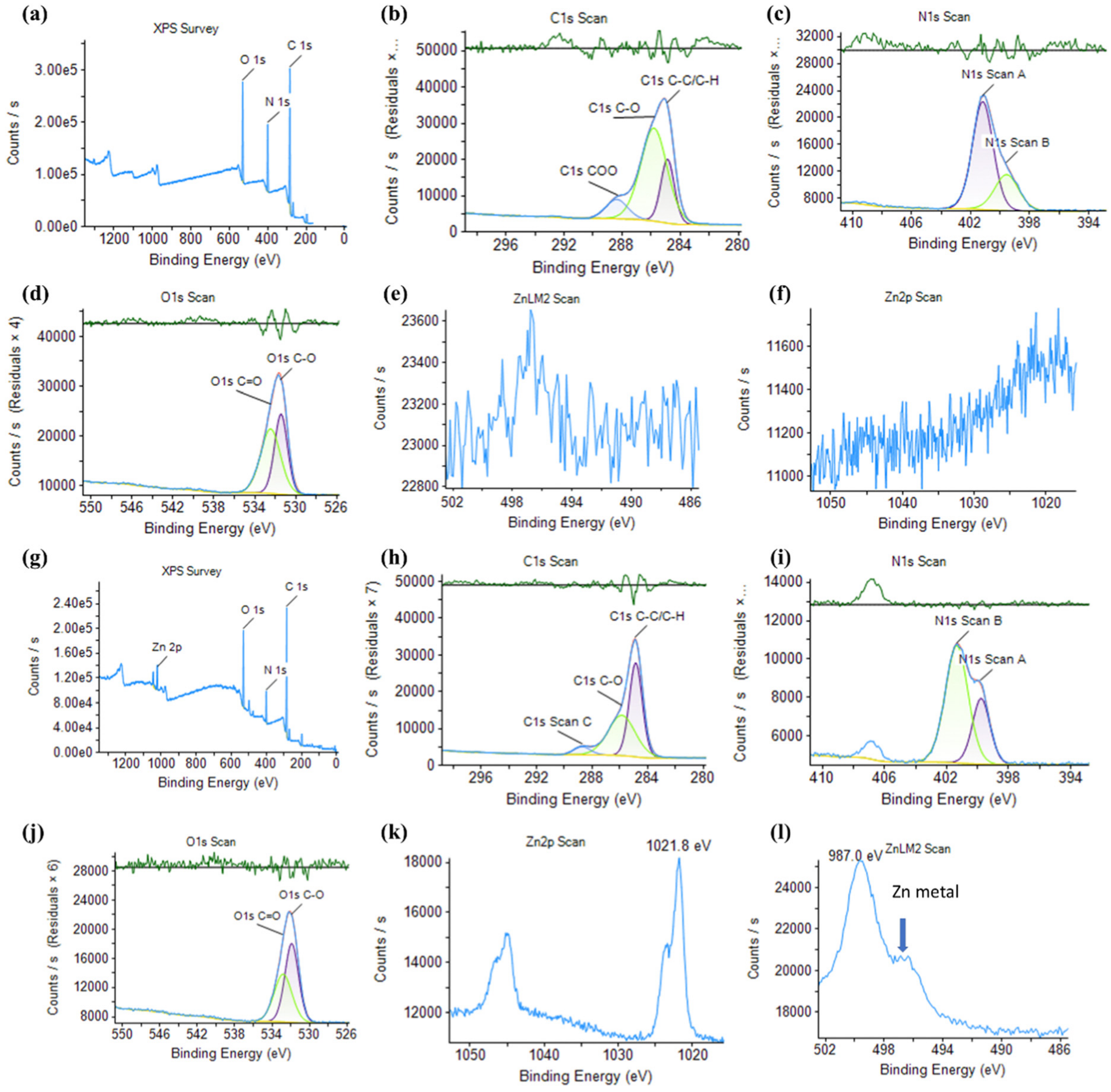

Fig. 2 (a) The entire XPS spectrum of the NCDs (b–f) High resolution of XPS spectrum of the NCDs: (b) C 1s, (c) N 1s, (d) O 1s, (e) Zn Lm2, and (f) Zn 2P. (g) The entire XPS spectrum of the Zn-NCDs. (h)–(l) High-resolution XPS spectrum of the Zn-NCDs: (h) C 1s, (i) N 1s, (j) O 1s, (k) Zn 2P, and (l) Zn 2P spectra of the Zn-NCDs.

284.6 eV, 286.1 eV, and 288.8 eV representing C–C/C=C, C–O/C–N, and C–O/C=N, respectively. In the high-resolution N_{1s} spectrum, the binding energy peak at 399.9 eV indicated that pyridinic N was the dominant state (Fig. 2c), suggesting that some N was doped in defect areas or near the edges of the graphitized carbon structure of NCDs. Fig. 2d shows the O_{1s} high-resolution spectrum, which consisted of two peaks at 531.6 and 533.1 eV, representing C–O and C=O, respectively.[54] The functional peaks observed in the XPS spectrum indicated the NCDs to contain large conjugated domains. Also, Zn scan of the NCDs sample (Fig. 2e and f) detected no Zn was in the XPS analysis, indicating that the NCDs were pure without any contamination of Zn. XPS analysis was also used to investigate the surface attachment of the Zn in Zn-NCDs nanomaterials. As shown in Fig. 2g, the XPS survey scan showed peaks at 284.8, 400.5, 498.6, 532.8, 1024, and 1045 eV associated with the presence of C_{1s} (66.7%), N_{1s} (10.9%), O_{1s} (16.4%), and Z_{n2p} (1.9%), respectively, confirming the presence of C, N, O, and Zn. As shown in Fig. 2h–l, the high-resolution XPS spectra over the deconvolution revealed different binding sites for C, N, O, and Zn. The high-resolution XPS scan of C_{1s} reveals deconvolution of several C_{1s} at 283.1 (C–Zn), 284.2 (C=C or C–C), 285.9 (C–O and C=O), and 287.9 eV (COO^-) (Fig. 2i). According to the N_{1s} deconvolution, two N-binding sites were found at 400.5 eV (pyridinic N) and 401.9 eV (doped N in graphitic carbon of Zn-NCDs) (Fig. 2j).[55] Similarly, different binding sites for C and Zn were observed at 529.5 eV (O–Zn), 530.9 eV (C–O), 531.8 eV (C=O), and 532.9 eV (COO–) (Fig. 2k).[56] In Fig. 2k, Zn 2p scans are shown, with $Zn_{2p3/2}$ at 1021.8 eV and $Zn_{2p1/2}$ at 1045.0 eV. According to Fig. 2l, the short scans of Zn in Zn-NCDs at 499.8 eV explain the doping of ionic Zn as well as metallic Zn at 496.7 eV.[57] The doping of Zn was in the metallic form, but due to the small size of the Zn-NCDs, the surface zinc was oxidized and assumed a Zn^{2+} state while the inner core Zn was still metallic (marked by arrow in Fig. 2l).

The X-ray diffraction (XRD) peak at 22° illustrated the graphitic carbon lattice (002) structure with few disordered carbon atoms as shown in Fig. S4 (ESI†) and also, the very minor phase from 44 to 53° ascribed to the highly disordered carbon lattice (100) arrangement in the crystal system along with the fractional graphitization of N. In the case of the Zn-NCDs sample, we have observed very minor peak metallic zinc at 43.6 and 48°, which also claims that metallic clusters of Zn atoms are incorporated in NCDs.[56,58] The typical graphitic carbon diffraction usually appears at 26–27°, but the obtained pattern was showing diffraction at 22°, the shift of 2θ value may be attributed to the reduction in the ordered sp^2 layers in the NCDs, Zn-NCDs carbon structure. The crystallite size of the NCDs and Zn-CDs was assessed using the Scherrer formula (as depicted in eqn (2)), and the calculated crystallite size was 2 nm.

$$D = \frac{0.9\lambda}{\beta \cos \theta} \tag{2}$$

where as D is the crystallite size, λ is the wavelength of X-ray wavelength, 0.9 is a dimensionless shape factor, β is the full wave half maxima of peak broadening intensity, and θ is the XRD Bragg's angle. The calculated crystallite size of Zn-NCDs is also 2 nm. TEM analysis indicated that the NCDs and Zn-NCDs were mostly spherical and generally well-dispersed (Fig. 3). Fig. 3a and d show TEM images of NCDs and Zn-NCDs nanomaterials samples, corresponding to average sizes of 5.0 nm (Fig. 3c) and 6.0 nm (Fig. 3f), respectively. A high-resolution TEM image of the NCDs (Fig. 3b) revealed their crystalline nature, and the lattice spacing

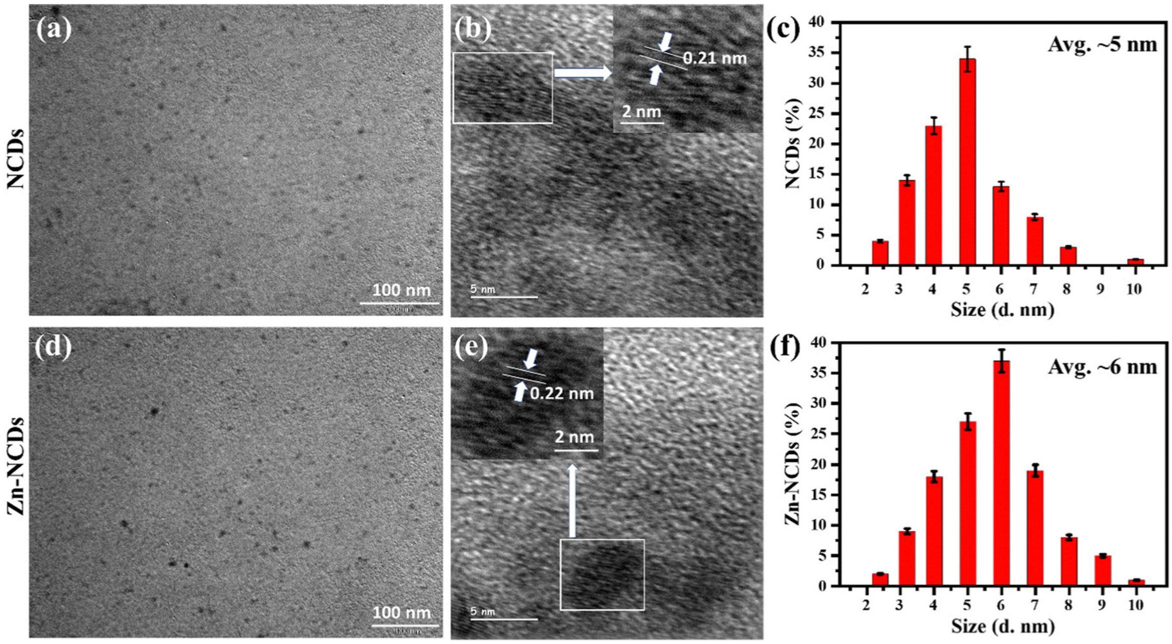

Fig. 3 The morphology of (a) TEM image of NCDs, (b) HRTEM image of NCDs with lattices, (c) particle size distribution of NCDs. (d) TEM image of Zn-NCDs. (e) HRTEM image of Zn-NCDs with lattices. (f) Particle size distribution histogram of Zn-NCDs.

was calculated using fast Fourier transformations (FFTs). We found the lattice spacing of NCDs to be 2.1 Å (∼64% of the time), attributed to graphene's lattice plane (100), which is reported to be close to 2.15 Å.[20] There were also values of 3.4 Å (∼10% of the time) related to graphite's (002) plane spacing and 2.6 Å (∼26% of the time) related to graphene's (112) plane spacing.[20] Although the lattice spacing of Zn-NCDs was close to graphite, the observed values were slightly more, attributed to Zn doping into the carbon core that may have caused lattice disorder.[57] Furthermore, these results indicate that the Zn-NCDs exhibit a preferential orientation (∼65% of the time) when on the grid, *i.e.* parallel to the grid plane. As shown in Fig. 3e, graphite spacing increased when samples showed aggregation. The purity of the histidine-derived NCDs and their Zn doping was also investigated by HRTEM-associated EDS analysis (Fig. 3b and e). NCDs were found to contain C, N, and O (Fig. S5a, ESI†), whereas Zn-NCDs contained C, N, O, and Zn (Fig. S5b, ESI†). Thus, the sample contained no impurities.

3.2. Cell viability study of the Zn-NCDs nanomaterials and live cell imaging

In order to design an effective antimicrobial agent that inhibits bacterial growth and biofilm formation, it is essential to strike a balance between efficiency and cytotoxicity. In this study, the MTT assay was performed *in vitro* to measure the cytotoxicity of NCDs and Zn-NCDs nanomaterials. The viability of HeLa cells was ∼93% (Fig. S6a, ESI†) and 88% (Fig. S6b, ESI†) when exposed to the highest concentrations of NCDs and Zn-NCDs (400 μg mL^{-1}), respectively. Although, as expected, the functionalization of NCDs with Zn resulted in slightly lower cell viability, overall NCDs and Zn-NCDs show low cytotoxicity.

We examined whether NCDs/Zn-NCDs were capable of intracellular fluorescence live cell imaging of HeLa cells. Native cells did not exhibit any fluorescence (Fig. 4a), whereas strong green fluorescence was observed using 50 μg mL^{-1} NCDs (Fig. 4b) or Zn-NCDs (Fig. 4c). The cells treated with NCDs and Zn-NCDs exhibit green fluorescence, as shown in Fig. 4b) and Fig. 4c). Moreover, no similar signal was observed in untreated control cells (Fig. 4a). As a result, cells treated with NCD nanomaterials exhibit slightly less fluorescence than cells treated with Zn-NCDs, and Zn-NCDs are distributed throughout the cell (Fig. 4c). Additionally, Zn-NCDs are typically nitrogen-doped carbon dots with the addition of zinc. The fluorescence properties of carbon dots mainly arise from their carbon core and surface functional groups, such as amino, hydroxyl, or carboxyl groups. Zinc itself does not typically exhibit any strong fluorescence properties. Therefore, we have observed slightly higher fluorescence intensity in Zn-NCDs with respect to regular NCDs (means without zinc). It is important to note that fluorescence imaging can be influenced by various factors, including the excitation wavelength, emission wavelength, quantum yield, and surface chemistry of the Zn-NCDs. Based on these results, it is evident that Zn-NCDs are capable of imaging the cytoplasm and nucleus of cells in live conditions as well. The XPS results indicate that NCDs/Zn-NCDs nanomaterials have many amino, carboxyl, and hydroxyl groups on their surfaces, suggesting that they are hydrophilic. We have also examined the three-dimensional projection of the cells treated with NCDs/Zn-NCDs nanomaterials using Z-stuck and observed that Zn-NCDs (Fig. 4e) are capable of entering both the cytoplasm and the nucleus, whereas NCDs (Fig. 4d) are capable of entering only the cytoplasm. Moreover, NCDs and Zn-NCDs have an average diameter of 5 nm and 6 nm, respectively, facilitating cellular penetration. Thus, NCDs/Zn-NCDs have a wide range of applications in biological imaging. Additionally, we have observed no HeLa cell (mammalian cell) was died during the incubation of NCDs/Zn-NCDs even after 24 h of treatment which explained that Zn-NCDs are considered to be non-toxic to mammalian cells. Because carbon dots are generally biocompatible and biodegradable as reported by several researcher.[24,51] Zn-NCDs, being carbon-based, can undergo degradation and metabolization within cells or in the body, minimizing any long-term accumulation or toxicity concerns. Zn-NCDs themselves possess low toxicity due to the properties of the constituent materials.[51] Carbon dots, which form the core of Zn-NCDs, are typically considered non-toxic and have been extensively investigated for various biomedical applications. However, it is important to note that the biocompatibility and mammalian cell toxicity of Zn-NCDs can still be influenced by factors such as concentration, exposure duration, and specific cell types.

3.3. Probing bacterial cell live imaging

In order to develop new antibacterial agents and to diagnose bacterial infections, it is crucial to identify bacterial strains.[59,60] Fluorescent dyes are often used to label pathogens, allowing their detection.[61] In order to overcome the limitations of conventional detection methods, many organic fluorescent probes have been designed.[61] In recent years, on/off fluorescent NCD probes, including NCDs, have been developed, allowing to image bacteria in real time and conduct quantitative analyses *in vitro* and *in vivo*.[62] Here, we tested the fabricated Zn-NCDs for bio-imaging of both Gram-positive and Gram-negative bacteria (Fig. 5). In most cases, as illustrated in Fig. 5b, after incubating *P. aeruginosa* with Zn-NCDs, different emission colours were visible under 488 nm excitation. The same experiment was performed with *S. aureus* and similar fluorescence was observed (Fig. 5d). The control samples, which were not treated with Zn-NCDs, did not display any noticeable fluorescence signals under the same conditions (Fig. 5a and c). Treating a mixture culture of *S. aureus* and *P. aeruginosa* bacteria with Zn-NCDs resulted good fluorescence in both types of bacteria (Fig. 5f), compared to no fluorescence in untreated bacteria (Fig. 5e). The results show that Zn-NCDs can be used as a probe for approximate visualized live and dead cell bacteria.

3.4. Antibacterial activity of the Zn-NCDs nanomaterials

The antimicrobial activity of quantum dots has recently attracted much attention due to the excellent optical properties, low toxicity to mammalian cells, and multivalent interaction capability with microorganisms of these strcutures.[63,64] The level of interaction between Zn-NCDs and bacterial cells depends on the composition, size, shape, and surface chemistry

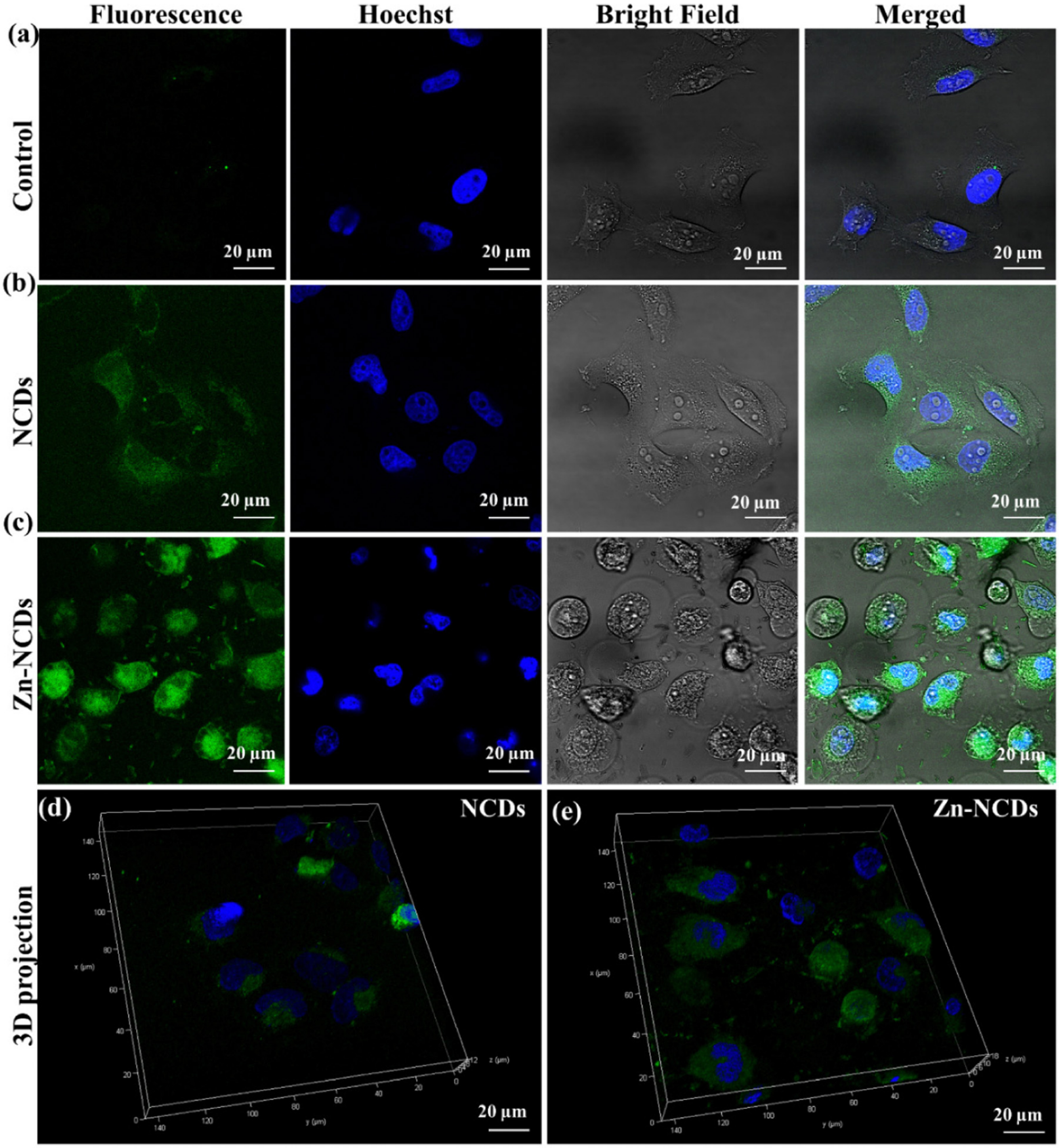

Fig. 4 Live cell imaging of HeLa cells (a) without any treatment, (b) following treatment with 50 µg mL^{-1} NCDs, and (c) following treatment with 50 µg mL^{-1} Zn-NCDs nanomaterials for 24 hours. Using Z-stuck, the following 3D-projection shows the HeLa cell with (d) NCDs, and (e) Zn-NCDs nanomaterials. Scale bar: 20 µm.

of the Zn-NCDs, as well as the structure and surface chemistry of the bacterial cells. The antibacterial activity of the Zn-NCDs nanomaterials has been studied using *P. aeruginosa*, *S. aureus*, and a mixture of the two strains and was studied using TEM measurements in the presence of NCDs/Zn-NCD nanomaterials. Fig. S7 (ESI†) depicts the TEM images of bacterial cells treated with Zn-NCDs nanomaterials for 24 hours under ambient conditions. In the control group of untreated *P. aeruginosa* (Fig. S7a and b, ESI†), *S. aureus* (Fig. S7e and f, ESI†), and a mixture of both bacteria (Fig. S7i and j, ESI†) many cells with a regular morphology and smooth surface were observed. As a result of the Zn-NCDs treatment, the number of bacterial cells in the *P. aeruginosa* (Fig. S7c and d, ESI†), *S. aureus* (Fig. S7g and h, ESI†), and mixed (Fig. S7k and l, ESI†) cultures decreased significantly, and the membranes of the bacterial cells appeared damaged. As a result of large-scale protein and cytoplasm leakage, the bacteria developed a light grey appearance, in contrast to the green colour of *P. aeruginosa*, the yellow colour of *S. aureus*, and the greenish-yellow colour of the mixture as a control (Fig. S8, ESI†). According to Fig. S8 (ESI†), cationic Zn-NCDs, spherical Zn-NCDs, and similar observations have been reported by several other researchers.[1,28,65–67] Fig. 4, which focuses on mammalian cells, likely illustrates the internalization mechanism of Zn-NCDs into these cells. There are several ways by which Zn-NCDs can enter

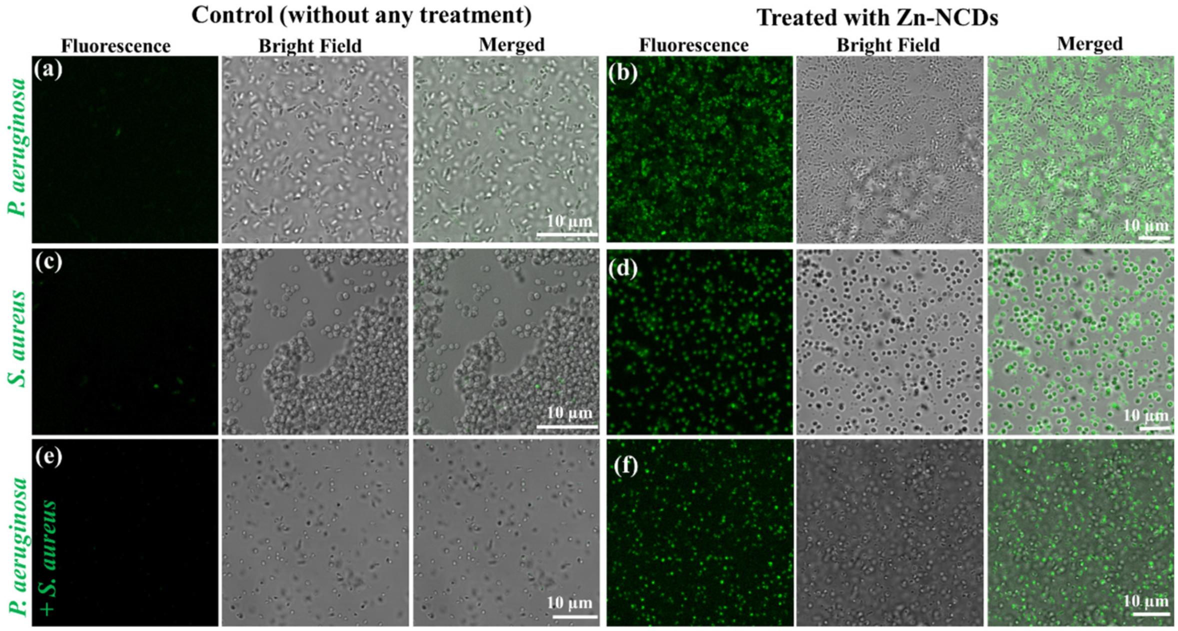

Fig. 5 Live cell imaging of a bacterial cells: (a) and (b) *P. aeruginosa*, (c) and (d) *S. aureus*, and (e) and (f) a mixture of *P. aeruginosa* and *S. aureus*. (a), (c) and (e) Untreated samples. (b) and (d) and (f) Following Zn-NCDs treatment for 12 hours.

mammalian cells, including endocytosis, direct membrane penetration, or receptor-mediated uptake. The specific mechanism by which Zn-NCDs enter mammalian cells would depend on their surface properties, size, positive charge, and functionalization. Similarly, Fig. 5 likely demonstrates Zn-NCD entry into bacterial cells. Bacterial cells have distinct characteristics compared to mammalian cells, including differences in the composition and structure of their cell membranes. Zn-NCDs can enter bacterial cells through mechanisms such as passive diffusion, membrane disruption, or active transport. Further, Zn-NCD induced obvious apoptosis of bacterial cells. NCDs and Zn-NCDs agglomerated in the treatment of *P. aeruginosa*, *S. aureus*, and the mixture of both bacteria (Fig. S9 and S10, ESI†). Moreover, Zn-NCDs nanoparticles (∼6 nm) have their small size as observed by HRTEM (Fig. 3) and high surface area, can exhibit enhanced antimicrobial activity compared to their bulk Zn based particles counterparts. When in contact with bacterial cells, Zn-NCDs nanoparticles can penetrate the cell membrane and release zinc ions, leading to similar mechanisms of damage as mentioned earlier.[29,35,36] The nanoparticles themselves can also cause physical damage to the bacterial cell membrane and biofilm growth inhibition by disrupting its integrity. In contrast, the NCDs/Zn-NCDs nanomaterials were adsorbing fairly uniformly around the cells, with some even within the cells (as shown in the confocal microscopy of Fig. 5). Therefore, there were significantly fewer residual cells than with NCDs/Zn-NCDs. Furthermore, Bacterial membrane pores are typically smaller, with diameters mostly less than 2 nm. As a result, the relatively larger size of Zn-NCDs may hinder their easy passage through these narrow channels. Moreover, in biological systems, the transport of materials across membranes is often regulated by various mechanisms to maintain the integrity and functionality of the cell. In the case of bacterial membranes, smaller molecules and ions can pass through the pores *via* passive diffusion or specific transport systems, while larger particles face difficulties in crossing the membrane. However, it's important to note that the ability of Zn-NCDs to pass through bacterial membrane pores can depend on various factors beyond just their size. Above antibacterial results were supported by studied the zone of inhibition in agarose plate. The Gram-positive *S. aureus* and Gram-negative *P. aeruginosa* were selected for testing the inhibitory zone. In Fig. S8a (ESI†) (*S. aureus*) and Fig. S8c (ESI†) (*P. aeruginosa*), the initial stages of adding treated or untreated filter paper to the LB plate are shown. Around filter papers treated with NCDs/Zn-NCDs, obvious inhibitory zones were observed for *S. aureus* (Fig. S8b, ESI†) and *P. aeruginosa* (Fig. S8d, ESI†). However, no inhibitory zones were observed around the control filter papers (no treatment with NCDs/Zn-NCDs). Based on Fig. 6m–o shows the removal of already formed biofilms by *P. aeruginosa* cells and *S. aureus* following another 24-hour incubation period with Zn-NCDs or NCDs. In addition, a higher biomass of biofilms was formed when *P. aeruginosa*, and S aureus strains were incubated for another 24 h without being treated with Zn-NCDs. The developed three sets of formed biofilms by above bacteria were treated with Zn-NCDs for study the amount of biofilm removal. Additionally, we have also added the experimental picture in Fig. S09–S11 (ESI†), *P. aeruginosa* and *S. aureus* cells as well as a mixture of *S. aureus* and *P. aeruginosa* biofilms were stained with crystal violet after treatment with/without Zn-NCDs. The first row of 96-well plate maintained their biofilm production without Zn-NCDs treatment. The removal of biofilms gradually increases with increasing treatment time. Fig. 6m–o, are clearly showing that reduction of formed biofilm quantity by Zn-NCDs nanomaterials as a function of time (0 h, 15 h, 18 h, 20 h, and 24 h). Zn-NCDs were used at different concentrations

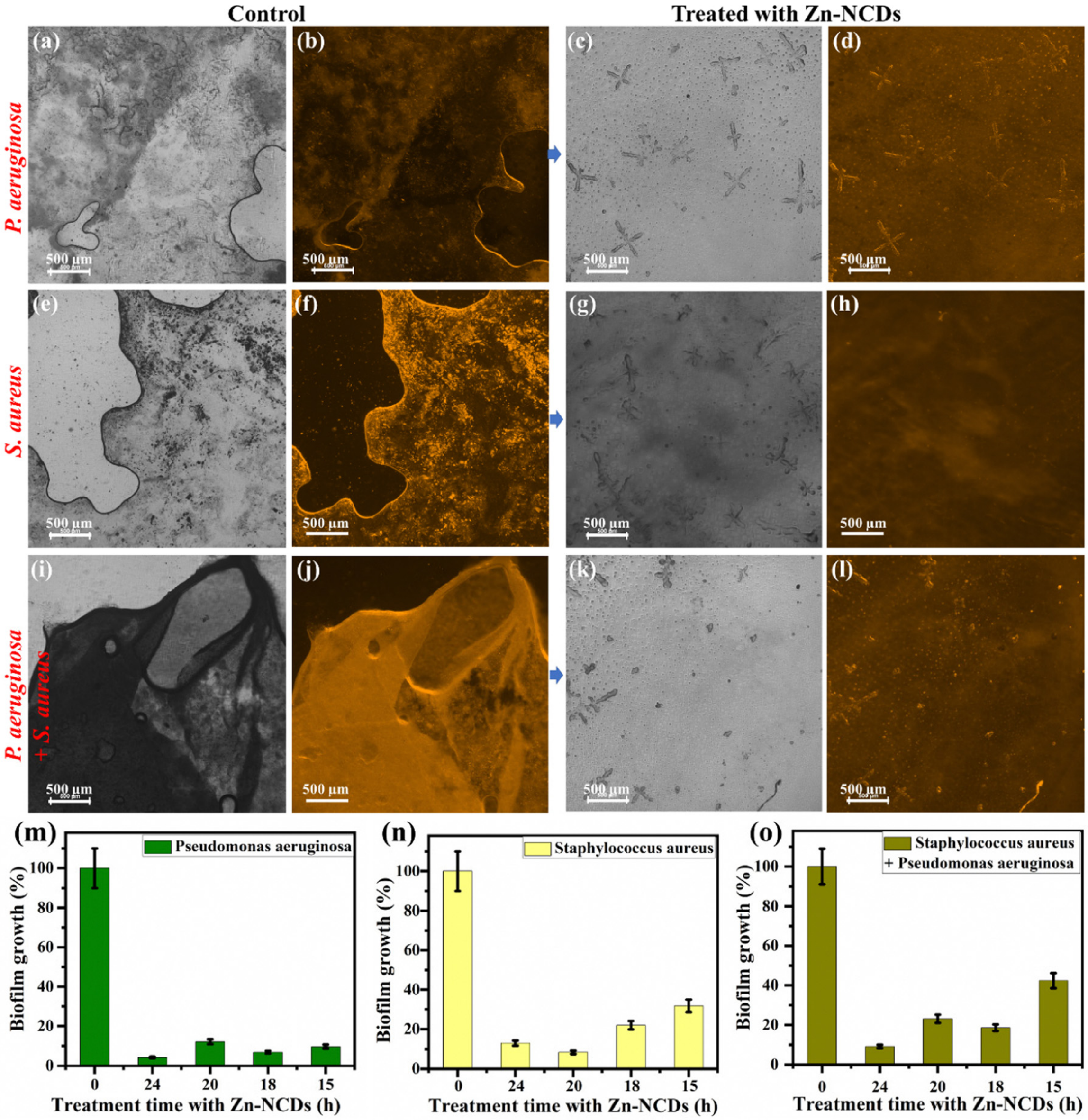

Fig. 6 (a)–(d) *P. aeruginosa*, (e)–(h) *S. aureus*, and (i)–(l) mixed culture biofilms. (a), (b), (e), (f), (i) and (j) Untreated control. (c), (d), (g), (h), (k) and (l) Following treatment with 100 µg mL^{-1} of Zn-NCDs. (a), (c), (e), (g), (i) and (k) Bright field. (b), (d), (f), (h), (j) and (l) Fluorescence images obtained at 670 nm under 590 nm excitation. Scale bar = 500 µm. (m–o) Inhibitory effect of Zn-NCDs nanomaterials on biofilms formed by (m) *P. aeruginosa*, (n) *S. aureus*, and (o) a mixture of both *S. aureus* and *P. aeruginosa*. The data are presented as mean ±SD (n = 3) with a significance level *$p < 0.05$.

(0–100 µg mL^{-1}) in this study, which influenced their efficacy and maximum biofilm degradation was observed with 100 µg mL^{-1} Zn-NCDs nanomaterials. Furthermore, NCDs/Zn-NCDs has demonstrated excellent antibacterial activity against *S. aureus* and *P. aeruginosa* by inhibition zone radius using statistical results analysis. Further, we observed a slightly better inhibition zone of bacteria for Zn-NCDs compared to NCDs. As a result, we continued to study the inhibition of bacteria and the inhibition of biofilm formation primarily using Zn-NCD nanomaterials.

3.5. Biofilm formation

Fig. S8a and b (ESI†) illustrates the formation of crystal violet-stained biofilms by *P. aeruginosa, S aureus*, and a combination of both *S aureus* and *P. aeruginosa* on an autoclave glass cover slides in 24 well plates. In all cases, discrete colonies developed during the initial phase of biofilm formation, however, in the mixture, we observed quick biofilm growth in *P. aeruginosa* and *S. aureus* single cultures. It appears that the structure of the biofilms that initially formed in mixture samples was similar in terms of the number of living cells by spectrophotometer OD analysis, but slightly differed in terms of thickness (6 ± 1 µm for mixture *versus* 4 ± 1 µm for *P. aeruginosa* and *S. aureus* alone) of biofilm. The thickness of the biofilm increased (6 ± 1 µm to 16 ± 2 µm) as the surface became uniformly covered with the biofilm formed by the mixture of both *S. aureus* and *P. aeruginosa* (Fig. S9g and h, ESI†). *P. aeruginosa*

(Fig. S9c and d, ESI†) and *S. aureus* (Fig. S9e and f, ESI†) formed uniform biofilms after 48 hours of incubation, and their thickness also increased (from 4 ± 1 μm to 12 ± 2 μm). However, it remained thinner than the biofilm formed by the mixture (Fig. S9g and h, ESI†). A similar experiment was performed using a 96-well spherical plate and excellent biofilm formation was observed (Fig. S10, ESI†).

3.6. Zn-NCDs penetrate/removal of biofilms and inhibit *S. aureus* and *P. aeruginosa* growth

Commonly-used drug particles cannot cross the grown biofilm, significantly reducing the effectivity of large-scale antibiotics. In order to conduct *in vitro* experiments on biofilm penetration/removal to kill *S. aureus* and *P. aeruginosa*, we constructed a biofilm model. A sterile cover glass slide was immersed in LB media followed by inoculation of *S. aureus* and *P. aeruginosa* bacteria cultured for 48 hours to form a biofilm. Following the successful formation of the biofilm, different concentrations of Zn-NCDs were added to the upper portion of the glass slide. As shown in Fig. S11a and b (ESI†), the growth of *P. aeruginosa*, *S. aureus*, and a mixture of both strains(P + S) was significantly inhibited, suggesting that Zn-NCDs could penetrate/remove the biofilm and inhibit bacterial growth. At concentrations below 50 μg mL^{-1}, Zn-NCDs had no obvious inhibitory effect on bacterial growth. Compared to the control, Zn-NCDs concentrations exceeding 50 μg mL^{-1} (most effectively 100 μg mL^{-1}) exhibited a significant antibacterial activity against the three tested cultures, while NCD nanomaterials exhibited a much less efficient inhibitory effect. Consequently, we hypothesized that Zn-NCDs could cross the biofilm and cause lethality to *P. aeruginosa* and *S. aureus* at higher concentrations (100 μg mL^{-1}). Microscopy analysis of the untreated control after 24 hours of incubation with *P. aeruginosa*, demonstrated the formation of a dense biofilm with many long stripes of fibres on the surface (Fig. 6a and b). Following treatment with different concentrations of NCDs/Zn-NCDs, small pores in the bacterial biofilm were observed. These small pores presumably facilitated the penetration of NCDs/Zn-NCDs into the biofilm. When the Zn-NCD concentration reached more than 50 μg mL^{-1}, the biofilm was severely destroyed (Fig. 6c and d). On the other hand, NCDs showed slightly milder effects on biofilms. Similar findings were observed for the formation of biofilms by *S. aureus* (Fig. 6e–h) and a mixture of *S. aureus* and *P. aeruginosa* (Fig. 6i–l). In the presence of 100 μg mL^{-1} Zn-NCDs, the biofilm was severely destroyed (Fig. 6g, h, k and l). Further, we have used the fluorescence imaging techniques and biofilm was stained with crystal violet for obtaining the thickness of the film (Fig. 6b, f and j) and also did the relative thickness measurement of biofilm growth by each set of bacteria, as described in Section 3.5. By combining multiple fluorescence imaging techniques and quantification of biofilm formation/inhibition have strengthen the evidence supporting the efficacy of Zn-NCDs in biofilm removal and gain a more nuanced understanding.

Biofilms are capable of encapsulating microorganisms and protecting them from being killed by drugs. Several types of biomolecules (polysaccharides, DNA, and peptides) contribute to the protective function of the extracellular matrix. As a result of the protective properties of biofilms, *P. aeruginosa* and *S. aureus* cells have long-term resistance and viability, making the treatment of oral diseases more challenging. The quantification of biofilm was done by semi-quantitative analysis using crystal violet staining. The working principle of biofilm quantification involves detecting decolorization in biofilms in order to determine the amount of biofilm produced by bacteria. Fig. 6m–o shows the removal of already formed biofilms by *P. aeruginosa* cells and *S. aureus* following another 24-hour incubation period with Zn-NCDs or NCDs. In addition, a higher biomass of biofilms was formed when *P. aeruginosa*, and S aureus strains were incubated for another 24 h without being treated with Zn-NCDs. The developed three sets of formed biofilms by the above bacteria were treated with Zn-NCDs to study the amount of biofilm removal. Additionally, we have also added the experimental picture in Fig. S12 (ESI†). *P. aeruginosa* and *S. aureus* cells as well as a mixture of *S. aureus* and *P. aeruginosa* biofilms were stained with crystal violet after treatment with/without Zn-NCDs. The first row of 96-well plates maintained their biofilm production without Zn-NCDs treatment. The removal of biofilms gradually increases with increasing treatment time. Fig. 6m–o, are clearly showing that reduction of formed biofilm quantity by Zn-NCDs nanomaterials as a function of time (0 h, 15 h, 18 h, 20 h, and 24 h). Zn-NCDs were used at different concentrations (0–100 μg mL^{-1}) in this study, which influenced their efficacy and maximum biofilm degradation was observed with 100 μg mL^{-1} We also would like to highlight that bar diagram (Fig. 6m–o) of treatment time Vs growth of biofilm inhibition slightly varying due to average out of the five different set of experiment. Despite the fact that NCDs have also inhibited the formation of biofilms, the effects of NCDs were slightly less pronounced than those of Zn-NCDs. Finally, we have observed that overall activity of biofilm inhibition is increasing with time of treatment with Zn-NCDs.

4. Conclusions and summary

We have studied the one-pot synthesis method as described for the preparation of histidine-derived Zn-NCDs as a means of inhibiting the growth of both Gram-positive (*S. aureus*) and Gram-negative (*P. aeruginosa)* bacteria as well as inhibiting biofilm formation. The synthesis method for Zn-NCDs did not require any additives, organic solvents, or further surface modification, making it a simple and scalable method for the synthesis of these materials. We found that NCDs and Zn-NCDs showed uniform sizes, were crystalline, photostable, and highly soluble in aqueous media. The structure, chemical composition, and low toxicity properties of the Zn-NCDs were demonstrated, and they were shown to be a promising novel material for the development of nano-level antibacterial drugs. Moreover, NCDs or Zn-NCDs could penetrate bacterial cell wall to further inhibit bacterial biofilm and bacterial growth. The antibacterial properties of the Zn-NCDs were tested against

S. aureus and *P. aeruginosa* using the agar well diffusion method and the inhibition of biofilm formation was evaluated using a crystal violet staining assay. The results showed that the Zn-NCDs had a slightly better antibacterial effect compared to the non-doped NCDs and were able to inhibit biofilm formation effectively by both *S. aureus* and *P. aeruginosa*.

Conflicts of interest

No conflict of interest has been declared by the authors.

Acknowledgements

V. B. K. is grateful to Tel Aviv University for the fellowship and financial support. The authors thank Dr Sigal Rencus-Lazar for language editing assistance.

References

1 S. B. Levy and M. Bonnie, *Nat. Med.*, 2004, **10**, S122–S129.
2 H. Nikaido, *Annu. Rev. Biochem.*, 2009, **78**, 119–146.
3 Y. A. Getahun, D. A. Ali, B. W. Taye and Y. A. Alemayehu, *Vet. Med.: Res. Rep.*, 2022, **13**, 173–190.
4 R. Vivas, A. A. T. Barbosa, S. S. Dolabela and S. Jain, *Microb. Drug Resist.*, 2019, **25**, 890–908.
5 WHO, *World Health Statistics.* World Health *2022*, 2022.
6 J. Larsen, C. L. Raisen, X. Ba, N. J. Sadgrove, H. Kerschner, P. Apfalter, R. Hartl and A. Deplano, *et al.*, *Nature*, 2022, **602**, 135–141.
7 P. C. Naha, Y. Liu, G. Hwang, Y. Huang, S. Gubara, V. Jonnakuti, A. Simon-Soro, D. Kim, L. Gao, H. Koo and D. P. Cormode, *ACS Nano*, 2019, **13**, 4960–4971.
8 H. Wang, S. Zhou, L. Guo, Y. Wang and L. Feng, *ACS Appl. Mater. Interfaces*, 2020, **12**, 39685–39694.
9 L. Guo, H. Wang, Y. Wang, F. Liu and L. Feng, *ACS Appl. Mater. Interfaces*, 2020, **12**, 21254–21262.
10 N. Shafran, I. Shafran, H. Ben-Zvi, S. Sofer, L. Sheena, I. Krause, A. Shlomai, E. Goldberg and E. H. Sklan, *Sci. Rep.*, 2021, **11**, 1–8.
11 E. A. Masters, B. F. Ricciardi, K. L. de, M. Bentley, T. F. Moriarty, E. M. Schwarz and G. Muthukrishnan, *Nat. Rev. Microbiol.*, 2022, **20**, 385–400.
12 J. Poovieng, B. Sakboonyarat and W. Nasomsong, *Sci. Rep.*, 2022, **12**, 1–12.
13 R. Kumar, V. B. Kumar and A. Gedanken, *Ultrason. Sonochem.*, 2020, **64**, 105009.
14 T. García-Mendiola, I. Bravo, J. M. López-Moreno, F. Pariente, R. Wannemacher, K. Weber, J. Popp and E. Lorenzo, *Sens. Actuators, B*, 2018, **256**, 226–233.
15 C. Ji, Y. Zhou, R. M. Leblanc and Z. Peng, *ACS Sens.*, 2020, **5**, 2724–2741.
16 K. Phukan, R. R. Sarma, S. Dash, R. Devi and D. Chowdhury, *Nanoscale Adv.*, 2022, **4**, 138–149.
17 Y. Yao, H. Zhang, K. Hu, G. Nie, Y. Yang, Y. Wang, X. Duan and S. Wang, *J. Environ. Chem. Eng.*, 2022, **10**, 107336.
18 P. Teng, J. Xie, Y. Long, X. Huang, R. Zhu, X. Wang, L. Liang, Y. Huang and H. Zheng, *J. Lumin.*, 2014, **146**, 464–469.
19 A. Kim, J. K. Dash, P. Kumar and R. Patel, *ACS Appl. Electron. Mater.*, 2022, **4**, 27–58.
20 V. B. Kumar, A. Borenstein, B. Markovsky, D. Aurbach, A. Gedanken, M. Talianker and Z. Porat, *J. Phys. Chem. C*, 2016, **120**, 13406–13413.
21 S. Kotta, H. M. Aldawsari and S. M. Badr-eldin, *Front. Mol. Biosci.*, 2020, **7**, 1–11.
22 Q. Jia, J. Ge, W. Liu, X. Zheng, S. Chen, Y. Wen, H. Zhang and P. Wang, *Adv. Mater.*, 2018, **30**, 1706090.
23 C. Liu, P. Zhang, X. Zhai, F. Tian, W. Li, J. Yang, Y. Liu, H. Wang, W. Wang and W. Liu, *Biomaterials*, 2012, **33**, 3604–3613.
24 V. B. Kumar, Z. Porat and A. Gedanken, *Nanomaterials*, 2022, **12**, 898.
25 K. Sato, R. Katakami, Y. Iso and T. Isobe, *ACS Appl. Nano Mater.*, 2022, **5**, 7664–7669.
26 D. Yoo, Y. Park, B. Cheon and M. H. Park, *Nanoscale Res. Lett.*, 2019, **14**, 272.
27 X. Li, Y. Fu, S. Zhao, J. Xiao, M. Lan, B. Wang, K. Zhang, X. Song and L. Zeng, *Chem. Eng. J.*, 2022, 133101.
28 Y. Zhang, X. Li, J. Li, M. Z. H. Khan, F. Ma and X. Liu, *BMC Chem.*, 2021, **15**, 1–12.
29 V. Puspasari, A. Ridhova, A. Hermawan, M. I. Amal and M. M. Khan, *Bioprocess Biosyst. Eng.*, 2022, **45**, 1421–1445.
30 R. J. Turner, *Microb. Biotechnol.*, 2017, **10**, 1062–1065.
31 J. Blichert-Toft, F. de Callataÿ, P. Télouk and F. Albarède, *Archaeol. Anthropol. Sci.*, 2022, **14**, 1–10.
32 A. Giumlia-Mair, *Adv. Archaeomater.*, 2020, **1**, 1–26.
33 A. Evans and K. A. Kavanagh, *J. Med. Microbiol.*, 2021, **70**, 001363.
34 J. a Lemire, J. J. Harrison and R. J. Turner, *Nat. Rev. Microbiol.*, 2013, **11**, 371–384.
35 P. Xia, S. Lian, Y. Wu, L. Yan, G. Quan and G. Zhu, *Vet. Res.*, 2021, 52.
36 S. Hussain, M. Khan, T. M. M. Sheikh, M. Z. Mumtaz, T. A. Chohan, S. Shamim and Y. Liu, *Front. Microbiol.*, 2022, 13.
37 Y. Wei, J. Wang, S. Wu, R. Zhou, K. Zhang, Z. Zhang, J. Liu, S. Qin and J. Shi, *Front. Immunol.*, 2022, **13**, 1–18.
38 S. N. Riduan and Y. Zhang, *Chem. – Asian J.*, 2021, **16**, 2588–2595.
39 L. H. Nguyen, T. T. Tran, L. T. N. Truong, H. H. Mai and T. T. Nguyen, *Biochemistry*, 2020, **59**, 1378–1390.
40 S. E. Mangion, A. M. Holmes and M. S. Roberts, *Int. J. Mol. Sci.*, 2021, **22**, 1–30.
41 N. L. Reeder, J. Xu, R. S. Youngquist, J. R. Schwartz, R. C. Rust and C. W. Saunders, *Br. J. Dermatol.*, 2011, **165**, 9–12.
42 A. Sirelkhatim, S. Mahmud, A. Seeni, N. H. M. Kaus, L. C. Ann, S. K. M. Bakhori, H. Hasan and D. Mohamad, *Nano Micro Lett.*, 2015, **7**, 219–242.
43 C. R. Mendes, G. Dilarri, C. F. Forsan, V. de, M. R. Sapata, P. R. M. Lopes, P. B. de Moraes, R. N. Montagnolli, H. Ferreira and E. D. Bidoia, *Sci. Rep.*, 2022, **12**, 1–10.

44 D. G. Conrady, C. C. Brescia, K. Horii, A. A. Weiss, D. J. Hassett and A. B. Herr, *Proc. Natl. Acad. Sci. U. S. A.*, 2008, **105**, 19456–19461.
45 A. Manuja, B. Kumar, R. Kumar, D. Chhabra, M. Ghosh, M. Manuja, B. Brar, Y. Pal, B. N. Tripathi and M. Prasad, *Toxicol. Rep.*, 2021, **8**, 1970–1978.
46 N. Kumar, P. Chamoli, M. Misra, M. K. Manoj and A. Sharma, *Advanced metal and carbon nanostructures for medical, drug delivery and bio-imaging applications*, Royal Society of Chemistry, 2022, vol. 14.
47 E. A. Permyakov, *Encyclopedia*, 2021, **1**, 261–292.
48 L. Zhou, S. Li, Y. Su, X. Yi, A. Zheng and F. Deng, *J. Phys. Chem. B*, 2013, **117**, 8954–8965.
49 Y. Chen, K. Tao, W. Ji, V. B. Kumar, S. Rencus-Lazar and E. Gazit, *Mater. Today*, 2022, **xxx**, 1–22.
50 H. Huang, C. Li, S. Zhu, H. Wang, C. Chen, Z. Wang, T. Bai, Z. Shi and S. Feng, *Langmuir*, 2014, **30**, 13542–13548.
51 V. B. Kumar, J. Sheinberger, Z. Porat, Y. Shav-Tal and A. Gedanken, *J. Mater. Chem. B*, 2016, **4**, 2913–2920.
52 M. E. Skogman, P. M. Vuorela and A. Fallarero, *J. Visualized Exp.*, 2016, **2016**, 1–10.
53 L. Lu, X. Han, J. Li, J. Hua and M. Ouyang, *J. Power Sources*, 2013, **226**, 272–288.
54 D. K. Khajuria, V. B. Kumar, D. Karasik and A. Gedanken, *ACS Appl. Mater. Interfaces*, 2017, **9**, 18557–18565.
55 A. A. Astafiev, A. M. Shakhov, A. G. Tskhovrebov, A. Shatov, A. Gulin, D. Shepel and V. A. Nadtochenko, *ACS Omega*, 2022, **7**, 6810–6823.
56 S. K. Tammina, Y. Wan, Y. Li and Y. Yang, *J. Photochem. Photobiol., B*, 2020, **202**, 111734.
57 Q. Xu, W. Cai, M. Zhang, R. Su, Y. Ye, Y. Li, L. Zhang, Y. Guo, Z. Yu, S. Li, X. Lin, Y. Chen, Y. Luo, J. Street and M. Xu, *RSC Adv.*, 2018, **8**, 17254–17262.
58 P. Khare, A. Bhati, S. R. Anand, Gunture and S. K. Sonkar, *ACS Omega*, 2018, **3**, 5187–5194.
59 S. W. Jun and Y. H. Ahn, *Nat. Commun.*, 2022, **13**, 1–8.
60 A. T. López-Jiménez and S. Mostowy, *Nat. Commun.*, 2021, **12**, 1–13.
61 S. A. Yoon, S. Y. Park, Y. Cha, L. Gopala and M. H. Lee, *Front. Chem.*, 2021, **9**, 1–19.
62 N. Kaur, P. Tiwari, N. Mate, V. Sharma and S. M. Mobin, *J. Photochem. Photobiol., B*, 2022, **229**, 112412.
63 S. Kumar, T. W. Kang, S. J. Lee, S. Yuldashev, S. Taneja, S. Banyal, M. Singhal, G. Ghodake, H. C. Jeon, D. Y. Kim and R. K. Choubey, *J. Mater. Sci.: Mater. Electron.*, 2019, **30**, 6977–6983.
64 S. Kumar, A. Jain, S. Panwar, I. Sharma, S. Gupta, M. Dopita and R. K. Choubey, *Appl. Phys. A: Mater. Sci. Process.*, 2023, **129**, DOI: 10.1007/s00339-023-06463-x.
65 J. Liu, J. Shao, Y. Wang, J. Li, H. Liu, A. Wang, A. Hui and S. Chen, *ACS Sustainable Chem. Eng.*, 2019, **7**, 16264–16273.
66 C. Bankier, R. K. Matharu, Y. K. Cheong, G. G. Ren, E. Cloutman-Green and L. Ciric, *Sci. Rep.*, 2019, **9**, 3–10.
67 H. Li, H. Jian, Y. Song, M. Zhang, H. Wang, F. Lu, H. Huang, Y. Liu, X. Dai, Z. Gu, Z. Yang, R. Zhou and Z. Kang, *ACS Appl. Mater. Interfaces*, 2018, **10**, 26936–26946.